Journal of Materials Chemistry A

PAPER

View Article Online
View Journal | View Issue

Cite this: J. Mater. Chem. A, 2019, 7, 13120

A cross-like hierarchical porous lithium-rich layered oxide with (110)-oriented crystal planes as a high energy density cathode for lithium ion batteries†

Min Chen,[a] Xiaojing Jin,[c] Zhi Chen,[a] Yaotang Zhong,[a] Youhao Liao,[ab] Yongcai Qiu,[abc] Guozhong Cao *[d] and Weishan Li *[ab]

Received 14th February 2019
Accepted 23rd April 2019

DOI: 10.1039/c9ta01708a

rsc.li/materials-a

Lithium-rich layered oxide (LLO) is a promising cathode for high energy density batteries due to its combined large specific capacity (>250 mA h g^{-1}) and high discharge voltage; however its application is limited by drawbacks including low rate capability, poor cycling stability and rapid voltage decay. To address these issues, a novel architecture, cross-like hierarchical porous LLO microsized aggregates made of ~100 nm primary particles with highly exposed (110) crystal planes, has been successfully developed by a morphology-conserved solid-state Li implantation method. Electrochemical performances demonstrate that the as-synthesized LLO exhibits a high initial capacity of 276 mA h g^{-1} at 0.1C, a remarkable rate capability of 143 mA h g^{-1} at 20C, a good cycling stability of 132 mA h g^{-1} after 300 cycles at 20C, and no significant voltage decay after 200 cycles at 0.5C. When it is coupled with a graphite anode, an energy density of 436 W h kg^{-1} (based on the total active materials of the cathode and anode) and an energy retention of 83% after 100 cycles are achieved. This architecture establishes a great strategy to engineer LLO for its application in high energy density batteries.

1. Introduction

High energy density batteries are of great interest to meet the growing demands in various applications such as portable electronics and electric vehicles.[1–8] Due to its high specific capacity (>250 mA h g^{-1}) and high discharge voltage (>3.5 V), lithium-rich layered oxide (LLO) with the formula of $xLi_2MnO_3\cdot(1-x)LiMO_2$ (M = Mn, Ni, Co, *etc.*) has been attracting much attention, and is composed of the intergrowth of the $LiMO_2$ phase ($R\bar{3}m$ space group) and Li_2MO_3-like phase ($C2/m$ space group).[9–17] However, there remain some challenges with this cathode, including low rate capability, poor cycling stability and rapid voltage decay.[18–20] To mitigate these issues, various strategies have been proposed and investigated, such as surface coating,[21–25] element doping,[26–30] nanocrystallization,[31] and morphology control.[32–38]

A micro/nanosized porous structure is important, since not only can the nanosized particles of cathode materials provide short ion transport paths and efficient active mass–electrolyte contact, but the porous structure also releases the strain generated during repeating charge/discharge processes. The unique architecture also reduces agglomeration upon cycling and decreases interfacial contact resistance. Additionally, the electrode materials comprising micro/nanostructures possess a higher tap density compared with the single nanoparticle counterparts, showing great potential for commercial applications.[39] Recently, considerable efforts on micro/nanostructure porous cathodes have been made by morphology-conserved method based Li implantation into precursors in a solid-state reaction.[33,34] The precursors can usually be prepared with tailored morphologies, which are then transcribed to the final products,[34,40,41] but it is still a challenge to tailor the precursor morphologies to be beneficial for performance delivery and exhibit high stability. Designing cathode materials with preferentially oriented crystal planes is another attractive approach, because some crystal planes provide an open structure for charge transfer while others do not.[42–46] In a layered cathode material for lithium ion intercalation/de-intercalation, for example, the crystal plane (110) in the hexagonal layered α-$NaFeO_2$ structure offers an open channel for lithium ion

[a]School of Chemistry and Environment, South China Normal University, Guangzhou 510006, China. E-mail: liwsh@scnu.edu.cn

[b]National and Local Joint Engineering Research Center of MPTES in High Energy and Safety LIBs, Engineering Research Center of MTEES (Ministry of Education), Key Lab. of ETESPG(GHEI), South China Normal University, Guangzhou 510006, China

[c]School of Environment and Energy, South China University of Technology, Guangzhou 510006, China

[d]Department of Materials Science and Engineering, University of Washington, Seattle, Washington 98195, USA. E-mail: gzcao@u.washington.edu

† Electronic supplementary information (ESI) available. See DOI: 10.1039/c9ta01708a

intercalation/de-intercalation and charge transfer. However, it is difficult to develop such active planes because they are highly unstable during preparation processes.[43,45,46]

In this work, we report a novel configuration, cross-like hierarchical porous LLO with highly oriented (110) planes (CHP-LMNO), *via* Li source implantation of the manganese–nickel oxide originating from thermal decomposition of a cross-like structured manganese–nickel oxalate precursor. This unique hierarchical porous architecture with highly exposed (110) planes has been verified by means of various spectroscopic techniques, and electrochemical measurements reveal its excellent properties and performance as a cathode for high energy density batteries. The as-prepared CHP-LMNO exhibits better rate capability compared with conventional counterpart sample (denoted as LMNO) and can deliver a high capacity as high as 143 mA h g^{-1} at a discharge rate of 20C. Moreover, when it is coupled and assembled in a full cell with a graphite anode, an energy density of 436 W h kg^{-1} (based on the mass of the cathode and anode active material) and a retention of 83% after 100 cycles have been achieved. These results demonstrated here represent an opportunity for the commercial application of lithium-rich materials.

2. Results and discussion

2.1 Material structure and composition

The morphologies of the synthesized products were investigated by scanning electron microscopy (SEM). As shown in Fig. 1a–c, the resulting LLO obviously exhibits a cross-like hierarchical porous architecture. To our knowledge, LLOs with common spherical-like and rod-like morphologies have been reported but this unique morphology has not been described in the previous reports.[20,32,43,45–47] The magnified SEM image in Fig. 1b shows the cross-like LLOs with an average length of about 5 μm and width of roughly 800 nm, consisting of numerous subunit nanoparticles of approximately 100 nm (inset in Fig. 1b). The hierarchical porous structure was further determined by Bruner–Emmett–Teller (BET) measurement (Fig. S1†). The pore sizes are distributed from 2 nm to 200 nm. The tap density of the as-prepared cross-like hierarchical porous LLO is ~2.0 g cm^{-3}, higher than that of the conventional counterpart sample of ~1.8 g cm^{-3} described in the following Experimental section. The energy dispersive X-ray spectroscopy (EDS) quantitative results (Fig. 1g–i) from three different selected areas are almost identical, suggesting the uniform distribution of Mn, Ni, and O elements. The atomic ratios of Mn and Ni from EDS are verified and agree with the results from inductively coupled plasma atomic emission spectroscopy (ICP-AES, Table S1,† Mn : Ni = 2.3 : 1). The elemental maps of a single cross (Fig. 1d–f) show that Mn, Ni, and O are homogeneously distributed in CHP-LMNO.[22]

The microstructure of the CHP-LMNO was characterized by transmission electron microscopy (TEM) and high resolution TEM (HRTEM). Fig. 2a further shows the resulting LLOs with a hierarchical porous cross-like structure. The primary nanoparticles in the magnified TEM image (Fig. 2b) have a hexagonal shape with a particle size of ~100 nm and the edge of each particle is clear. The HRTEM (Fig. 2c) image of the region marked by a green rectangle in Fig. 2b shows noticeable lattice fringes with a lattice distance of 0.42 nm which is assigned to

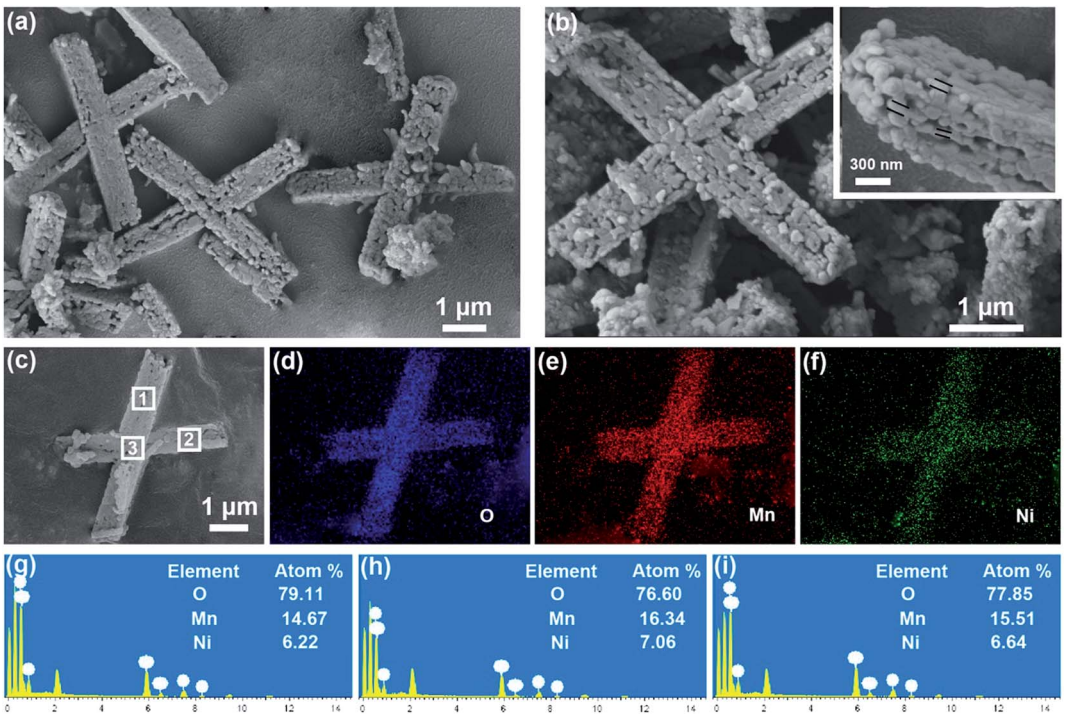

Fig. 1 (a and b) SEM images of CHP-LMNO, (c) the SEM image of an individual cross-like CHP-LMNO, (d–f) element maps, and (g–i) EDS results of CHP-LMNO in three selected areas of 1, 2 and 3 in (c).

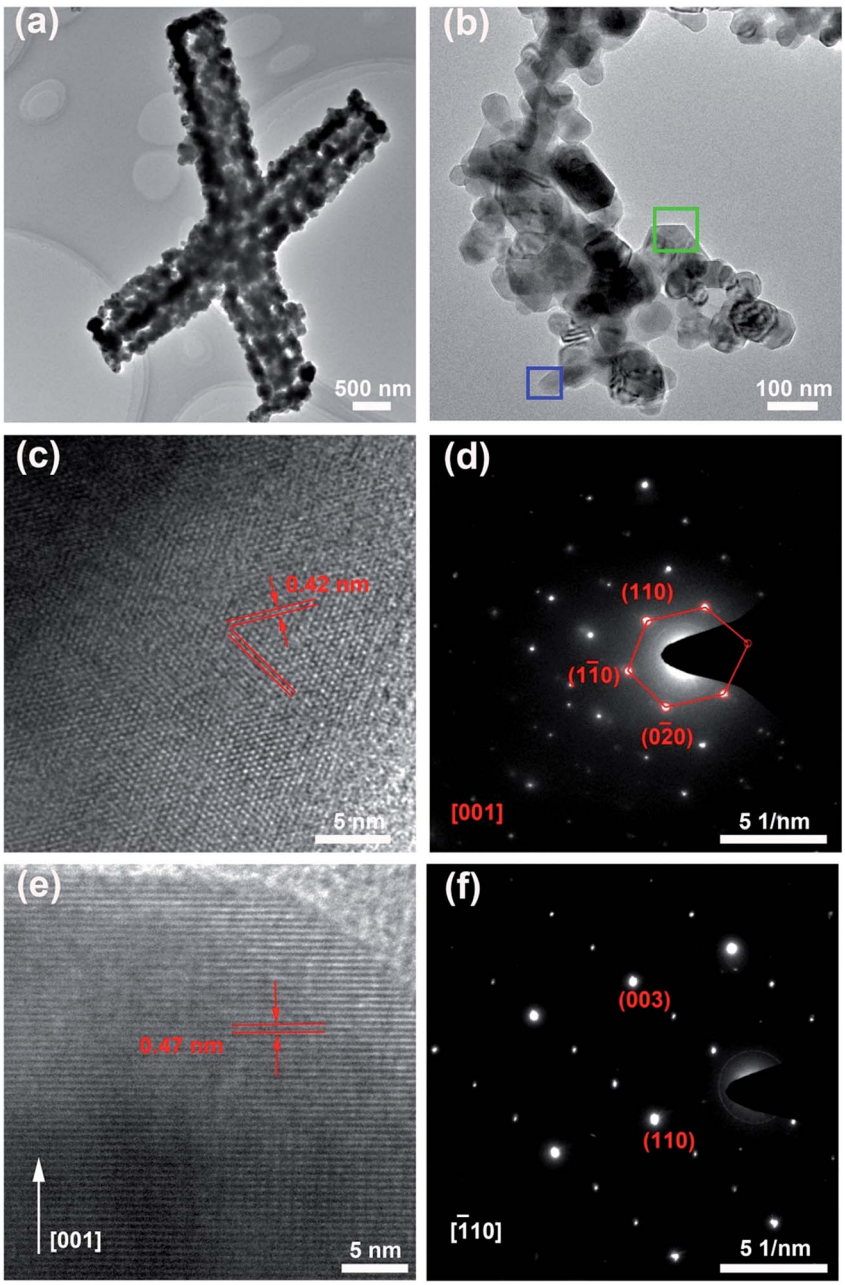

Fig. 2 (a and b) TEM images of CHP-LMNO; the green and blue rectangular areas in (b) show the frontal and lateral planes of a single nanoparticle, (c) the HRTEM image and (d) SAED pattern of the frontal plane shown in the green rectangular area, and (e) the HRTEM image and (f) SAED pattern of the lateral plane shown in the blue rectangular area.

the (020) planes of the monoclinic Li_2MnO_3.[32,37,43,48] The corresponding selected area electron diffraction (SAED) pattern (Fig. 2d) represents a superposition of the hexagonal $R\bar{3}m$ space group of the $LiMO_2$ phase and the monoclinic $C2/m$ space group of the Li_2MnO_3 phase, which reflects an alternately ordered arrangement of lithium ions and transition-metal (TM) cations in the TM layer along the c axis in the $LiMO_2$ array.[32,37,46,49] The above results indicate that the frontal plane of the nanoparticles is the (003) plane of the $LiMO_2$ phase and the (001) plane of the Li_2MnO_3 phase;[32,43,50] therefore the lateral planes will be perpendicular to the (001) plane that belongs to {010} planes in the hexagonal unit cell. Fig. 2e displays the lattice fringes of a lateral plane with an interplanar spacing of 0.47 nm, which can be ascribed to the distance between TM layers of $LiMO_2$ along the [001] direction.[45,46,51] These observed characteristics reveal that the lateral plane of the nanoparticles belongs to {010} planes, and the further determination of the SAED pattern (Fig. 2f) demonstrates that it is the (−110) plane.[43,45,46,51] The morphology in SEM images and the microstructure in the TEM image all reveal that the designed LLO has a cross-like hierarchical porous structure with an exposed {010} plane.

The crystallographic phase of the as-prepared samples was also analyzed using power X-ray diffractometer (XRD) measurement. Fig. 3a shows the typical XRD pattern of LLO. The observed strong peaks can be indexed to the α-$NaFeO_2$ structure with a space group symmetry of $R\bar{3}m$ (PDF#09-0063) and several weak peaks around 20–25° can be assigned to a monoclinic system with the space group $C2/m$ (PDF#27-1252), which reflects the ordering of lithium ions in the TM layer.[52,53] In addition, the pair peaks of (006)/(012) and (018)/(110) in Fig. 3b and c clearly split in the XRD patterns indicate the resulting LLO with a highly ordered layered structure.[28,54,55] The (110) plane has an open layered interspace for Li^+ ions to intercalate into the bulk of LLOs, but there is no straight tunnel for the (018) plane due to the dense stacking of atoms in this plane, as shown in the inset of Fig. 3c.[45] The ratio of $I_{(110)}/I_{(018)}$ being more than 1 further demonstrates CHP-LMNO with (110)-oriented active planes.[46] The refined hexagonal lattice parameters are displayed in Table S1.† The hierarchical porous CHP-LMNO with active planes will provide a more unhindered pathway for Li^+ transport, thus enhancing the reactive kinetics and the porous structure accommodates enough space to buffer volume changes during repeated cycling. The Raman spectrum in Fig. 3d displays that CHP-LMNO contains three peaks near 600, 484 and 432 cm^{-1}, which correspond to two Raman active vibrations of A_{1g} and E_g in LLOs with $R\bar{3}m$ symmetry and a fingerprint vibration of the superlattice, respectively.[56] In general, A_{1g} represents the symmetrical stretching of M–O and E_g represents symmetrical deformation. The strongest peak near 605 cm^{-1} corresponds to A_{1g} without any splitting indicating a uniform layered structure in CHP-LMNO. The peak around 488 cm^{-1} corresponds to E_g and a small peak at 430 cm^{-1} originates from the Mn-rich region in the Li_2MnO_3-like $C2/m$ structure.[42,50] To investigate chemical states, X-ray photoelectron spectroscopy (XPS) was also carried out (Fig. 3e and f). The observed peak bonding energies of Ni 2p and Mn 2p are 854.9 eV and 642.3 eV, respectively, which are in good agreement with Ni^{2+} and Mn^{4+} reported in the LLOs.[47,57,58]

For comparison, a sample with microsphere morphology (LMNO) was also prepared by co-precipitation and characterized with XRD, TEM, SEM, and ICP. The obtained results are displayed in Fig. S2 and Table S1.† It can be found that there are no obviously oriented crystal planes in the LMNO sample. As seen in Table S1,† there is no significant difference in chemical composition between LMNO and CHP-LMNO. Therefore, any differences in electrochemical performance between the two samples should be attributed to their different structure.[39,59,60]

2.2 Formation process of CHP-LMNO

In order to understand the formation process of CHP-LMNO, the morphologies and crystal structures of the precursor were also characterized by SEM, XRD and FTIR. The SEM image of the precursor (Fig. S3†) exhibits a cross-like structure with an average length of ~5 μm and width of ~800 nm for each rod. The XRD pattern and FTIR spectrum of the precursor are displayed in Fig. S4 and S5.† The primary peaks can be indexed to the mixed phases of $MnC_2O_4\cdot 2H_2O$ and $NiC_2O_4\cdot 2H_2O$. When pre-calcined at 450 °C, the $MC_2O_4\cdot xH_2O$ can be easily transformed into manganese–nickel oxide *via* dehydration and release of carbon oxides.[33] After thermal decomposition, the structure with the cross-like shape is preserved and the surface becomes rough, as shown in Fig. S6a.† The Mn : Ni ratio in the oxides from EDS (Fig. S6b†) is about 2.3 : 1, which is well in agreement with the results of ICP (Table S1†) but lower than the mole ratio of $MnCl_2$ (0.15 M) : $Ni(NO_3)_2$ (0.05 M) for the preparation of oxalates. This discrepancy can be ascribed to the better solubility of manganese oxalate than of nickel oxalate in ethanol and deionized water used for filtration, which causes the partial loss of manganese. The Mn : Ni ratio from EDS (Fig. S6b†) is in good agreement with that of the final products of 0.583 : :0.250 (Table S1†). The selected elemental maps for O, Mn, and Ni in Fig. S6c–e† show that the elements are uniformly distributed.

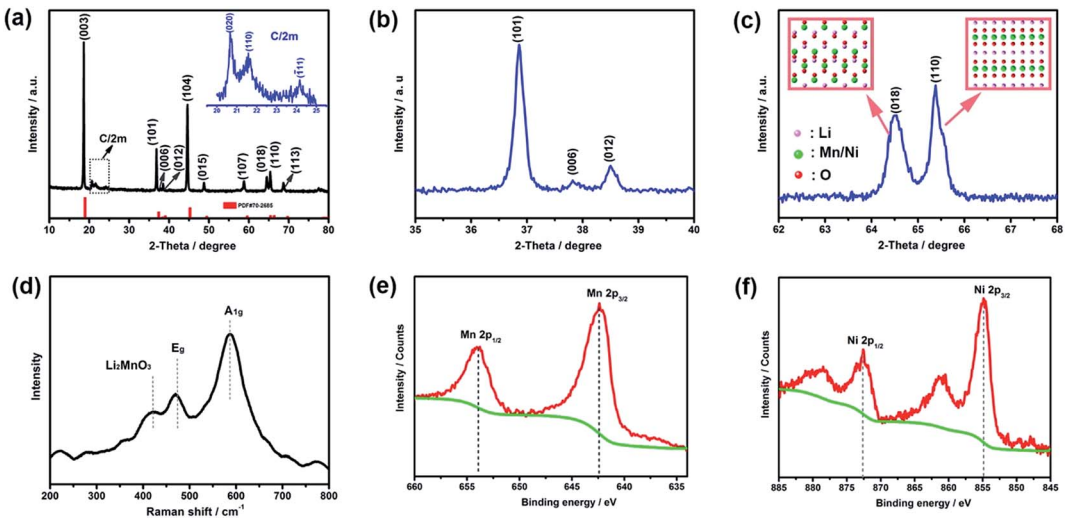

Fig. 3 (a) XRD patterns of CHP-LMNO and local magnification (b and c and inset in a), (d) Raman spectrum of CHP-LMNO, and (e and f) the typical XPS patterns for Mn 2p (e) and Ni 2p (f) of CHP-LMNO.

The oxalate group as a bidentate bridging ligand is known to play an important role in interlinking metal ions, giving rise to a chain-like structure.[32,47] The numerous chain-like structures act as building blocks which assemble *via* molecular interactions.[61–63] In the present study, the interaction between metal ions and oxalate groups is vital for the cross-like morphology. When only $MnCl_2 \cdot 4H_2O$ was present in the system during the reaction, the solid products had a heterogeneous cuboid shape (Fig. S7a†). After calcination and Li and Ni source implantation, the final products would not retain the cuboid morphology with aggregated particles (Fig. S7c†). When $Ni(NiO_3)_2 \cdot 6H_2O$ was used as a single component to coordinate with oxalate, the morphology of the product had an irregular uniaxial shape made of nanorods (Fig. S7b†), and the final product remained as irregular shaped particles after calcination and Li and Mn source implantation (Fig. S7d†). Although the exact formation mechanism is unknown at the moment, the experimental data and results strongly indicate that the presence and coexistence of both $MnCl_2 \cdot 4H_2O$ and $Ni(NiO_3)_2 \cdot 6H_2O$ are critical for the formation of the cross-like morphology. Different attractive interactions in the growth orientation possibly exist and the direct anisotropic growth kinetics of the metal oxalate promote the formation of the cross-like shape during the microemulsion reaction/synthesis. The oriented plane can be assigned to the surfactant cetyltrimethyl ammonium bromide (CTAB) with hydrophilic groups adsorbed on some crystallized planes which change the surface energy.[42,61,63–65] Due to the oriented growth kinetics of the metal oxalate nanostructure and surface passivation by CTAB, the cross-like structure in this case is thought to be a result of their synergic action. The formation of hierarchical porous CHP-LMNO consists of two sequential steps: (1) the cross-like precursor preferentially forms during the microemulsion reaction; (2) CHP-LMNO inherits the morphology of the precursor and is endowed with a porous structure in the thermal decomposition process due to the release of CO_2 and H_2O. Fig. 4 schematically illustrates the whole formation process.

2.3 Electrochemical performance of CHP-LMNO

The first charge and discharge curve (Fig. 5a) of CHP-LMNO shows that the initial discharge capacity is ~276 mA h g^{-1} at 0.1C (where 1C = 250 mA g^{-1}), which is higher than the 260 mA h g^{-1} for LMNO. As seen from the charge plots of CHP-LMNO and LMNO, both samples exhibit a slope region below 4.5 V, assigned to Li^+ extraction from the $LiMO_2$ phase accompanied by the oxidation of $Ni^{2+}/Ni^{3+}/Ni^{4+}$ and a long plateau region around 4.5 V, corresponding to the activation of Li_2MnO_3 accompanied by the irreversible loss of oxygen.[66,67] More visible distinctness in the initial charge process is identified from the differential charge curves (dQ/dV) in Fig. 5b. For CHP-LMNO, the first oxidation peak at around 3.83 V is ascribed to the oxidation process of Ni^{2+} to Ni^{3+}, the following peak at around 4.09 V is assigned to the oxidation of Ni^{3+} to Ni^{4+}, and the third sharp oxidation peak at 4.56 V is normally associated with irreversible oxidation and decomposition of the electrolyte.[24,39] However, all oxidation peaks of LMNO shift slightly towards high voltage, which indicates that LMNO suffers a more serious polarization compared with the CHP-LMNO.[68]

The prolonged cycling performance was evaluated at a charge/discharge rate of 0.5C for 200 cycles. Prior to charge/discharge at 0.5C, the cells were activated for 5 cycles at 0.1C. Fig. 5c displays the cycling stability and corresponding coulombic efficiency of the two samples. The CHP-LMNO sample can deliver a discharge capacity of 231 mA h g^{-1} and maintain a capacity retention of 94% after 200 cycles, but only 208 mA h g^{-1} and 72% for the LMNO. In the charge/discharge curve profiles of the 200th cycle (Fig. 5d), the gap between the charge and discharge plateau in CHP-LMNO is obviously smaller than that in LMNO. The much smaller gap of CHP-LMNO implies lower polarization and minor structural transformation, indicating that the material can achieve better electrochemical performance. The specific discharge curves and voltage decay are clearly exhibited in Fig. 5e and f. The sample of CHP-LMNO shows a much slower voltage decay percentage of

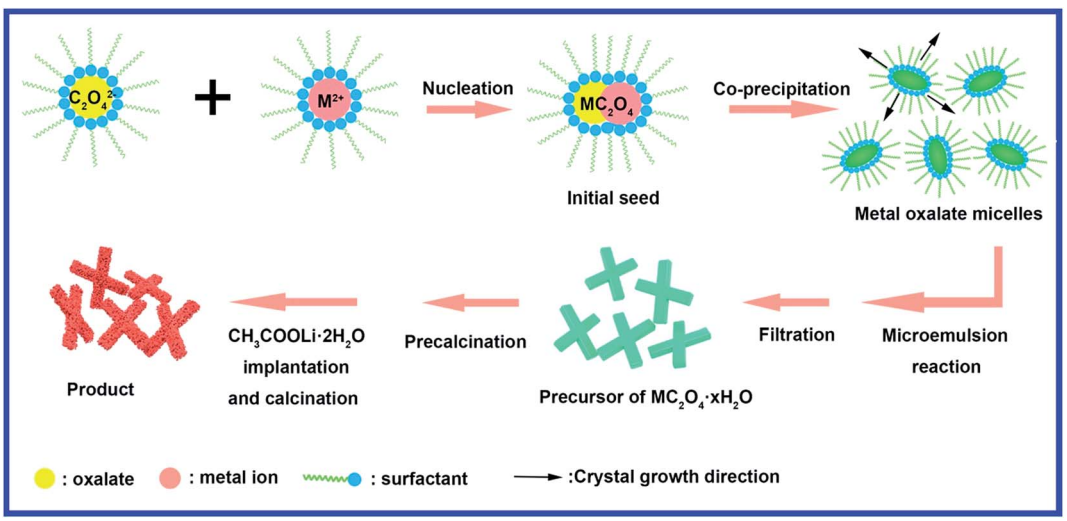

Fig. 4 Schematic illustration of the microemulsion reaction coupled with subsequent Li implantation for the formation process of LLO with a cross-like hierarchical porous structure.

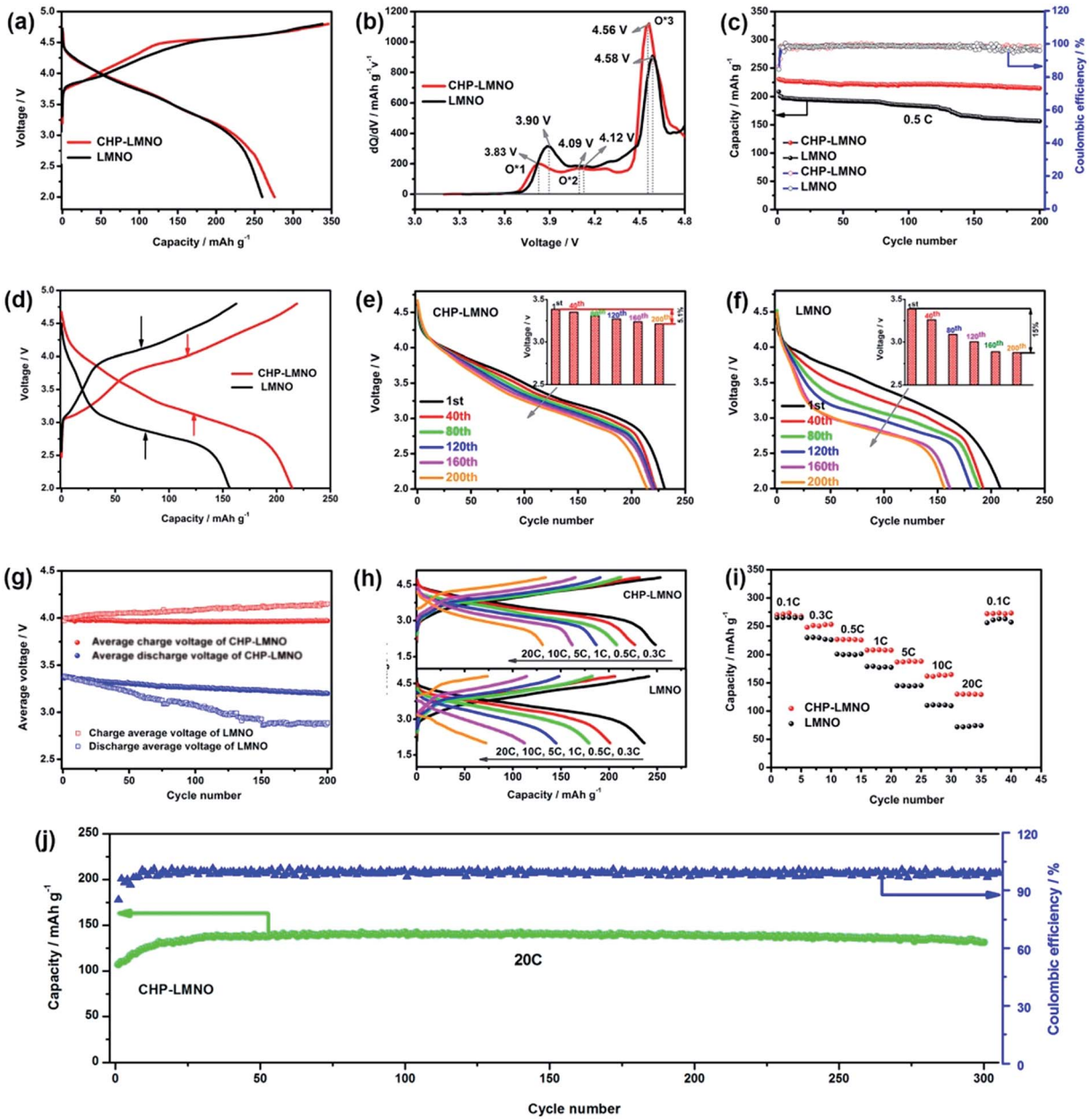

Fig. 5 (a) Initial charge/discharge curves of CHP-LMNO and LMNO at 0.1C (1C = 250 mA g^{-1}) in the voltage range of 2.0–4.8 V and (b) the corresponding dQ/dV curves of the initial charge process; (c) cycling stability and corresponding coulombic efficiency of CHP-LMNO and LMNO at 0.5C (after 5 cycles of activation at 0.1C); (d) the charge/discharge curves of CHP-LMNO and LMNO at the 200th cycle; (e and f) the selected discharge curves at 0.5C and the corresponding average discharge voltage for CHP-LMNO and LMNO; (g) the average charge and discharge voltage of CHP-LMNO and LMNO; (h) the charge/discharge curves of CHP-LMNO and LMNO at various rates; (i) rate capability of CHP-LMNO and LMNO; (j) long-term cycling performance and corresponding coulombic efficiency of CHP-LMNO at 20C.

5.1% compared with the 15% of LMNO from the initial to terminal cycle. As seen in Fig. 5g, the average charge voltage of LMNO is higher than that of CHP-LMNO and gradually increases with cycling, while its average discharge voltage is lower than that of CHP-LMNO and decays seriously, indicating the lower polarization and the better structural stability of CHP-LMNO. These results suggest that the porous micro/nano-structured electrode material CHP-LMNO can endure long-term cycling and resist structural evolution.[69,70] As seen from the reduction process, more clear voltage decay can be noticed in the dQ/dV plots of the two samples (Fig. S8†). The first reduction peak (Re1) around 4.5 V involves the reduction of O^{n-} ($n < 2$);[71] the second reduction peak (Re2) around 3.5 V is related to the reduction of Ni^{4+}/Ni^{2+}, corresponding to Li occupation in octahedral sites; the third reduction peak (Re3) less than 3.5 V can be explained by the reduction of Mn^{4+}/Mn^{3+}.[58] The Re3 peaks in LMNO obviously shift to low voltage, which is also attributed to more serious structural transformation from layers to spinel.[26,39,47,50] Fig. S9† presents the SEM images of CHP-LMNO and LMNO after 200 cycles. For LMNO, the morphology

becomes indiscernible and the aggregated particles crack into a few pieces. However, CHP-LMNO preserves the essential cross-like morphology after long cycling, indicating that CHP-LMNO might be used as a long cycling cathode material. XRD (Fig. S10†) was also applied to identify the inner structure of CHP-LMNO and LMNO after cycling. Compared with standard diffraction, the peaks around 20–25° disappear for both samples, which could be explained by the initial irreversible oxygen loss. For the other peaks, CHP-LMNO displays more pronounced peaks than LMNO, especially for peaks (003) and (104), indicating that LMNO undergoes more severe destruction in structural integrity. Raman spectra of CHP-LMNO and LMNO after cycling were also obtained to identify their structural evolution. As seen from Fig. S11,† the symmetrical stretching peak for A_{1g} of the cycled samples shifts to a higher wavelength than that for the fresh material (Fig. 3d). This peak can be split into two peaks around 630 cm^{-1} and 580 cm^{-1}, corresponding to the A_{1g} vibration mode in the spinel and layered structure, respectively.[53] Based on the peak area, the contents of these phases can be estimated. The spinel in the cycled LMNO constitutes 43% but constitutes only 24% in the cycled CHP-LMNO, further confirming the integrity of the layered structure in CHP-LMNO.

The rate capabilities were measured at various current densities and the charge and discharge tests were carried out with the same current density at each rate. The selected charge and discharge voltage profiles of CHP-LMNO and LMNO at 0.3C, 0.5C, 1C, 5C, 10C and 20C rates are displayed in Fig. 5h. The capacity drops in CHP-LMNO at high current rates are much gentler when compared with those in LMNO. Fig. 5i shows the continuous cycling result at incremental current densities from 0.1C to 20C then recovering to 0.1C. The discharge capacities of the CHP-LMNO are higher than those of LMNO especially at high rates. The CHP-LMNO can achieve the highest discharge capacity of 143 mA h g^{-1} at 20C (Fig. 5j) and shows excellent cycling stability with a capacity retention of 92% relative to the highest capacity after 300 cycles. The coulombic efficiency of CHP-LMNO is retained at more than 99%, indicating the good reversibility at a high current rate. Such good rate capability can be ascribed to the unique hierarchical porous structure of CHP-LMNO with highly oriented planes, which provides facile Li^+ transport tunnels and reduces the Li^+ diffusion pathways, thus providing more rapid charge transfer and higher current is obtained in a short time.[42–46] The enhanced Li^+ intercalation/deintercalation kinetics was further evaluated using electrochemical impedance spectra (Table S2 and Fig. S12†). A material with a porous structure exposes more surfaces, which might be more liable to form spinel-like structures and cause the voltage decay and deteriorate the rate capability of the material. This drawback can be avoided in the porous CHP-LMNO, because its surface is rich in (110)-oriented crystal planes, which exhibit fast Li^+ intercalation/deintercalation kinetics, prevent the formation of spinel-like structures and suppress voltage decay. Importantly, the electrochemical performances of CHP-LMNO are better than those of most samples that have been reported in the literature (Table S3†).

2.4 Full cell demonstration

The remarkable electrochemical performances of CHP-LMNO indicate that the hierarchical porous CHP-LMNO cathode is suitable for application in high power/density LIBs or even in full cells.[72] To further demonstrate the electrochemical properties in a full cell, CHP-LMNO was coupled with a graphite anode to assemble the full cell. Fig. 6a schematically shows the structure of the full cell. The initial charge and discharge curve

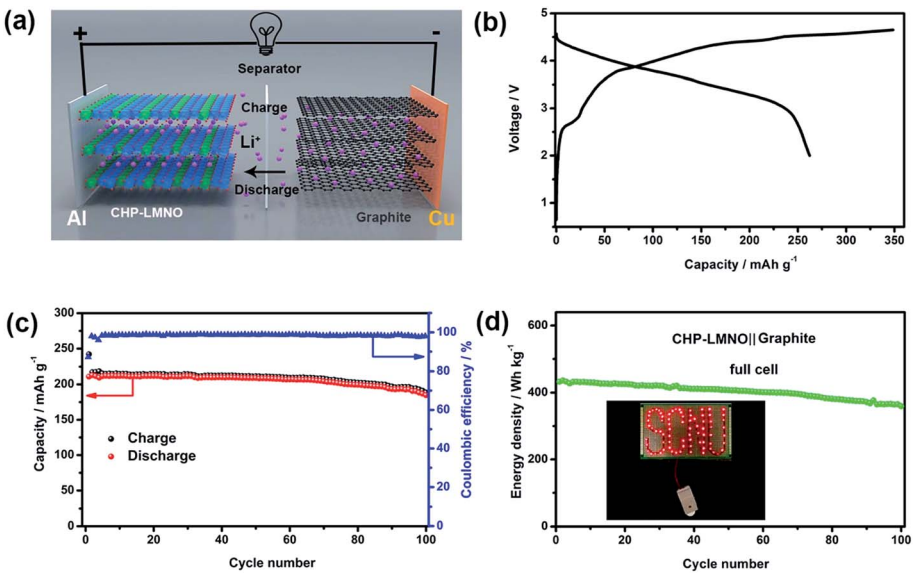

Fig. 6 (a) Schematic representation of the full cell (CHP-LMNO||graphite); (b) the initial charge/discharge plot of the full cell at 0.1C (1C = 200 mA h g^{-1}) in the voltage range of 2.0–4.65 V; (c) the cycling performance and coulombic efficiency of the full cell at 1C. (d) Energy density and lighting demonstration of the full cell.

at 0.1C (where 1C = 200 mA h g^{-1}) of the full cell is exhibited in Fig. 6b. Specifically, the full cell can deliver a discharge capacity as high as 262 mA h g^{-1} with an initial coulombic efficiency of 75%. The plot also exhibits a slope region below 4.45 V and a plateau region around 4.5 V, which shows the similar Li^+ deintercalation behavior in half and full cells.[73,74] The cycling stability was further confirmed by long-term cycling at 1C. Before testing at 1C, the full cell was activated for 5 cycles at 0.1C. Fig. 6c and d show the cycling and energy density performance. The full cell can deliver a high capacity of 213 mA h g^{-1}, corresponding to an energy density of 436 W h kg^{-1} (based on the mass of cathode and anode active materials) at 1C and a capacity retention of 83% after 100 cycles. Impressively, the assembled full cell CHP-LMNO‖graphite can power a "SCNU" log consisting of 76 light emitting diodes (LEDs, 1.7 V, 60 mW each) in parallel connection. The excellent performance of the as-prepared CHP-LMNO can be attributed to the following reasons:[31,34,37,45,46] (1) the unique hierarchical structure can enhance the surface area thus providing sufficient active sites; (2) the porous structure facilitates electrolyte infiltration and provides more buffer space; (3) the highly (110)-oriented plane enables much easier Li^+ migration.

3. Conclusion

In conclusion, a novel cross-like hierarchical porous layered lithium-rich oxide with highly (110)-oriented planes has been successfully prepared *via* a morphology-conserved method and was applied as a cathode material for high energy density LIBs. The CHP-LMNO notably improves the long cyclability of the electrode and exhibits a remarkably high reversible capacity and excellent rate capability. In particular, CHP-LMNO can also suppress voltage decay during cycling. What is more, in the full cell, CHP-LMNO still maintains good electrochemical performance with a high discharge capacity of 213 mA h g^{-1} at 1C and a corresponding energy density of 436 W h kg^{-1} (based on the total cathode and anode active material). Therefore, CHP-LMNO, as a novel high power/energy density cathode material, might also be applicable for ameliorating the electrochemical properties of LLOs.

4. Experimental section

4.1 Preparation of CHP-LMNO and LMNO

Firstly, 5 g CTAB was dissolved in a mixture of 150 mL cyclohexane and 5 mL of *n*-pentanol under magnetic stirring for 30 min. Subsequently, 5 mL of a 0.8 M $H_2C_2O_4 \cdot 2H_2O$ aqueous solution was added to the above solution under stirring for an additional 1 h until the mixture solution became transparent, denoted as solution A. Finally, 5 mL of an aqueous solution B containing 0.15 M $MnCl_2 \cdot 4H_2O$ and 0.05 M $Ni(NO_3)_2 \cdot 6H_2O$ was added dropwise into solution A under stirring. The mixture was stirred for 16 h at room temperature. The laurel-green solid $MC_2O_4 \cdot H_2O$ precursor was obtained by filtering and washing several times with ethanol and deionized water, and then dried in a vacuum oven at 120 °C for 10 h. The manganese–nickel oxide was synthesized by calcining $MC_2O_4 \cdot H_2O$ at 450 °C for 5 h. The final product CHP-LMNO was obtained by implanting 5 wt% excess $CH_3COOLi \cdot 2H_2O$ into manganese–nickel oxide at 800 °C for 12 h. For comparison, the counterpart LLO was also synthesized by a co-precipitation method, and denoted as LMNO. In brief, a stoichiometric amount of $MnSO_4 \cdot 7H_2O$ and $NiSO_4 \cdot 6H_2O$ was dissolved in 50 mL deionized water. 2 M NaOH and a measurable amount of $NH_3 \cdot H_2O$ was added into the above solution under vigorous magnetic stirring. Subsequently, the mixture solution was heated to 50 °C and the pH was maintained at 11. After continuous co-precipitation for 16 h, the $M(OH)_2$ precursor was filtered, washed with deionized water, and dried in a vacuum oven at 120 °C for 10 h. The resulting precursor was pre-calcined at 450 °C for 5 h to obtain manganese–nickel oxide and then mixed with 5 wt% excess $CH_3COOLi \cdot 2H_2O$. After mechanical mixing, the final product LMNO was obtained by annealing the solid mixture at 800 °C for 12 h in an air atmosphere.

4.2 Structural characterization

The morphologies of the prepared precursors (manganese–nickel oxalate and manganese–nickel oxide) and the final products (CHP-LMNO and LMNO) were observed by SEM (ZEISS Ultra 55 and JEOL JSM-6380, Japan). Their microstructures were investigated by TEM and HRTEM (FEI Tecnai F20, USA). EDS and ICP-AES were used to detect the content of the metal ions. The tap density of CHP-LMNO and LMNO was roughly measured in a graduated cylindrical centrifuge tube by continuously tapping till the volume value remained the same. The crystal structure of the obtained samples was investigated by XRD (Rigaku UltimaIV, Japan) with Cu-Kα radiation in the 2θ degree range from 10° to 80° with a scanning step of 5° min^{-1}. The layered structure was clarified using Raman microscope (LabRAM Aramis, France) at 532 nm excitation. Chemical states of the resulting composition were analyzed using an XPS (Genesis2000). Basic vibrations of the groups in the precursor were analyzed by FTIR (Nicolet 6700). The textural properties were obtained using N_2-adsorption/desorption measurement at 77 K on a BET analyzer (Micromeritics ASAP 2020 M). The total surface area was characterized by the BET method and the corresponding pore distribution was calculated by the Barrett–Joyner–Halenda (BJH) method.

4.3 Electrochemical measurements

CR 2025 type button cells were assembled in a glove box (MBraun, Germany) in an argon-filled atmosphere (H_2O, O_2 < 1 ppm). The cathode electrode was fabricated by casting blending slurry on the surface of Al foil, which contained 80 wt% CHP-LMNO or LMNO, 10 wt% polyvinylene difluoride (PVdF), and 10 wt% acetylene black in *N*-methyl pyrrolidone (NMP). The anode electrode was prepared by daubing a mixture of 80 wt% graphite, 10 wt% Super-P and 10 wt% PVDF in NMP onto a Cu current collector. The prepared films were dried in a vacuum oven at 120 °C overnight. Li foil and a graphite electrode were used as the counter electrode in the half and full cell. The areal loadings of the cathode and graphite anode were about 3.0 and 2.0 mg cm^{-2}, respectively. An excess capacity of about 6% of the

graphite anode was considered to fully utilize the cathode. 1 M $LiPF_6$ dissolved in EC, DMC, and EMC (1 : 1 : 1 in volume) was used as the electrolyte and a single layer PP membrane (Celgard 2300) was used as the separator. The electrochemical measurements were estimated on a battery test system (LAND CT 2001A, China) at room temperature (25 °C). The galvanostatic charge/discharge tests were carried out at different current rates in the range of 2.0–4.8 V (*vs.* Li^+/Li) in the half cell and 2.0–4.65 V in the full cell. Electrochemical impedance spectroscopy (EIS) was performed on an Autolab (PGSTAT-30, Eco Chemie B.V. Company) with an amplitude of 0.005 V in the frequency range from 100 kHz to 0.1 Hz.

Conflicts of interest

There are no conflicts to declare.

Acknowledgements

This work was supported by the National Natural Science Foundation of China (Grant No. 21872058) and the Key Project of Science and Technology in Guangdong Province (2017A010106006).

References

1 C. Zhan, T. Wu, J. Lu and K. Amine, *Energy Environ. Sci.*, 2018, **11**, 243–257.
2 G. Assat and J.-M. Tarascon, *Nat. Energy*, 2018, **3**, 373–386.
3 L. Xing, X. Zheng, M. Schroeder, J. Alvarado, A. von Wald Cresce, K. Xu, Q. Li and W. Li, *Acc. Chem. Res.*, 2018, **51**, 282–289.
4 W. Liu, P. Oh, X. Liu, M. J. Lee, W. Cho, S. Chae, Y. Kim and J. Cho, *Angew. Chem., Int. Ed.*, 2015, **54**, 4440–4457.
5 P. K. Nayak, E. M. Erickson, F. Schipper, T. R. Penki, N. Munichandraiah, P. Adelhelm, H. Sclar, F. Amalraj, B. Markovsky and D. Aurbach, *Adv. Energy Mater.*, 2018, **8**, 1702397.
6 B. Liao, H. Li, M. Xu, L. Xing, Y. Liao, X. Ren, W. Fan, L. Yu, K. Xu and W. Li, *Adv. Energy Mater.*, 2018, **8**, 1800802.
7 P. Hou, J. Yin, M. Ding, J. Huang and X. Xu, *Small*, 2017, **13**, 1701802.
8 L. Wang, J. L. Shi, H. Su, G. Li, M. Zubair, Y. G. Guo and H. Yu, *Small*, 2018, **14**, 1800887.
9 J. Wang, X. He, E. Paillard, N. Laszczynski, J. Li and S. Passerini, *Adv. Energy Mater.*, 2016, **6**, 1600906.
10 Y.-L. Ding, J. Xie, G.-S. Cao, T.-J. Zhu, H.-M. Yu and X.-B. Zhao, *Adv. Funct. Mater.*, 2011, **21**, 348–355.
11 X. Li, K. Zhang, D. Mitlin, Z. Yang, M. Wang, Y. Tang, F. Jiang, Y. Du and J. Zheng, *Chem. Mater.*, 2018, **30**, 2566–2573.
12 J. Xu, F. Lin, M. M. Doeff and W. Tong, *J. Mater. Chem. A*, 2017, **5**, 874–901.
13 A. Singer, M. Zhang, S. Hy, D. Cela, C. Fang, T. A. Wynn, B. Qiu, Y. Xia, Z. Liu, A. Ulvestad, N. Hua, J. Wingert, H. Liu, M. Sprung, A. V. Zozulya, E. Maxey, R. Harder, Y. S. Meng and O. G. Shpyrko, *Nat. Energy*, 2018, **3**, 641–647.
14 S. Kim, M. Aykol, V. I. Hegde, Z. Lu, S. Kirklin, J. R. Croy, M. M. Thackeray and C. Wolverton, *Energy Environ. Sci.*, 2017, **10**, 2201–2211.
15 H. Yu, R. Ishikawa, Y. G. So, N. Shibata, T. Kudo, H. Zhou and Y. Ikuhara, *Angew. Chem., Int. Ed.*, 2013, **52**, 5969–5973.
16 M. Ko, P. Oh, S. Chae, W. Cho and J. Cho, *Small*, 2015, **11**, 4058–4073.
17 X. Li, K. Zhang, D. Mitlin, E. Paek, M. Wang, F. Jiang, Y. Huang, Z. Yang, Y. Gong, L. Gu, W. Zhao, Y. Du and J. Zheng, *Small*, 2018, **14**, 1802570.
18 X. Yu, Y. Lyu, L. Gu, H. Wu, S.-M. Bak, Y. Zhou, K. Amine, S. N. Ehrlich, H. Li, K.-W. Nam and X.-Q. Yang, *Adv. Energy Mater.*, 2014, **4**, 1300950.
19 Y. Zhao, J. Liu, S. Wang, R. Ji, Q. Xia, Z. Ding, W. Wei, Y. Liu, P. Wang and D. G. Ivey, *Adv. Funct. Mater.*, 2016, **26**, 4760–4767.
20 Y.-D. Zhang, Y. Li, X.-Q. Niu, D.-H. Wang, D. Zhou, X.-L. Wang, C.-D. Gu and J.-P. Tu, *J. Mater. Chem. A*, 2015, **3**, 14291–14297.
21 X. D. Zhang, J. L. Shi, J. Y. Liang, Y. X. Yin, J. N. Zhang, X. Q. Yu and Y. G. Guo, *Adv. Mater.*, 2018, **30**, 1801751.
22 E. Zhao, X. Liu, H. Zhao, X. Xiao and Z. Hu, *Chem. Commun.*, 2015, **51**, 9093–9096.
23 Y. Liu, Z. Yang, J. Li, B. Niu, K. Yang and F. Kang, *J. Mater. Chem. A*, 2018, **6**, 13883–13893.
24 N. H. Vu, J. C. Im, S. Unithrattil and W. B. Im, *J. Mater. Chem. A*, 2018, **6**, 2200–2211.
25 F. Zheng, C. Yang, X. Xiong, J. Xiong, R. Hu, Y. Chen and M. Liu, *Angew. Chem., Int. Ed.*, 2015, **54**, 13058–13062.
26 R. Yu, Z. Zhang, S. Jamil, J. Chen, X. Zhang, X. Wang, Z. Yang, H. Shu and X. Yang, *ACS Appl. Mater. Interfaces*, 2018, **10**, 16561–16571.
27 W. K. Pang, H.-F. Lin, V. K. Peterson, C.-Z. Lu, C.-E. Liu, S.-C. Liao and J.-M. Chen, *Chem. Mater.*, 2017, **29**, 10299–10311.
28 B. Li, H. Yan, J. Ma, P. Yu, D. Xia, W. Huang, W. Chu and Z. Wu, *Adv. Funct. Mater.*, 2014, **24**, 5112–5118.
29 R. A. House, L. Jin, U. Maitra, K. Tsuruta, J. W. Somerville, D. P. Förstermann, F. Massel, L. Duda, M. R. Roberts and P. G. Bruce, *Energy Environ. Sci.*, 2018, **11**, 926–932.
30 A. Choi, J. Lim, H.-J. Kim, S. C. Jung, H.-W. Lim, H. Kim, M.-S. Kwon, Y. K. Han, S. M. Oh and K. T. Lee, *Adv. Energy Mater.*, 2018, **8**, 1702514.
31 J. Zheng, S. Myeong, W. Cho, P. Yan, J. Xiao, C. Wang, J. Cho and J.-G. Zhang, *Adv. Energy Mater.*, 2017, **7**, 1601284.
32 F. Fu, J. Tang, Y. Yao and M. Shao, *ACS Appl. Mater. Interfaces*, 2016, **8**, 25654–25659.
33 M. Chen, Y. Zhang, L. Xing, Y. Liao, Y. Qiu, S. Yang and W. Li, *Adv. Mater.*, 2017, **29**, 1607015.
34 J. Yang, F. Cheng, X. Zhang, H. Gao, Z. Tao and J. Chen, *J. Mater. Chem. A*, 2014, **2**, 1636–1640.
35 X. He, J. Wang, R. Wang, B. Qiu, H. Frielinghaus, P. Niehoff, H. Liu, M. C. Stan, E. Paillard, M. Winter and J. Li, *J. Mater. Chem. A*, 2016, **4**, 7230–7237.
36 W. Sun, Y. Li, Y. Liu, Q. Guo, S. Luo, J. Yang, C. Zheng and K. Xie, *J. Mater. Chem. A*, 2018, **6**, 14155–14161.

37 Y. Zhang, W. Zhang, S. Shen, X. Yan, A. Wu, J. Yin and J. Zhang, *J. Power Sources*, 2018, **380**, 164–173.
38 F. Fu, Y. Yao, H. Wang, G.-L. Xu, K. Amine, S.-G. Sun and M. Shao, *Nano Energy*, 2017, **35**, 370–378.
39 M. Chen, X. Xiang, D. Chen, Y. Liao, Q. Huang and W. Li, *J. Power Sources*, 2015, **279**, 197–204.
40 G. Ma, S. Li, W. Zhang, Z. Yang, S. Liu, X. Fan, F. Chen, Y. Tian, W. Zhang, S. Yang and M. Li, *Angew. Chem., Int. Ed.*, 2016, **55**, 3667–3671.
41 X. Zhang, F. Cheng, J. Yang and J. Chen, *Nano Lett.*, 2013, **13**, 2822–2825.
42 J. Zeng, Y. Cui, D. Qu, Q. Zhang, J. Wu, X. Zhu, Z. Li and X. Zhang, *ACS Appl. Mater. Interfaces*, 2016, **8**, 26082–26090.
43 L. Chen, Y. Su, S. Chen, N. Li, L. Bao, W. Li, Z. Wang, M. Wang and F. Wu, *Adv. Mater.*, 2014, **26**, 6756–6760.
44 G. Z. Wei, X. Lu, F. S. Ke, L. Huang, J. T. Li, Z. X. Wang, Z. Y. Zhou and S. G. Sun, *Adv. Mater.*, 2010, **22**, 4364–4367.
45 Y. Li, Y. Bai, C. Wu, J. Qian, G. Chen, L. Liu, H. Wang, X. Zhou and F. Wu, *J. Mater. Chem. A*, 2016, **4**, 5942–5951.
46 M. Xu, L. Fei, W. Zhang, T. Li, W. Lu, N. Zhang, Y. Lai, Z. Zhang, J. Fang, K. Zhang, J. Li and H. Huang, *Nano Lett.*, 2017, **17**, 1670–1677.
47 G. Wang, L. Yi, R. Yu, X. Wang, Y. Wang, Z. Liu, B. Wu, M. Liu, X. Zhang, X. Yang, X. Xiong and M. Liu, *ACS Appl. Mater. Interfaces*, 2017, **9**, 25358–25368.
48 Y.-P. Deng, F. Fu, Z.-G. Wu, Z.-W. Yin, T. Zhang, J.-T. Li, L. Huang and S.-G. Sun, *J. Mater. Chem. A*, 2016, **4**, 257–263.
49 F.-D. Yu, L.-F. Que, Z.-B. Wang, Y. Zhang, Y. Xue, B.-S. Liu and D.-M. Gu, *J. Mater. Chem. A*, 2016, **4**, 18416–18425.
50 M. Chen, D. Chen, Y. Liao, X. Zhong, W. Li and Y. Zhang, *ACS Appl. Mater. Interfaces*, 2016, **8**, 4575–4584.
51 L. Chen, Y. Su, S. Chen, N. Li, L. Bao, W. Li, Z. Wang, M. Wang and F. Wu, *Adv. Mater.*, 2014, **26**, 6756–6760.
52 Y. Zuo, B. Li, N. Jiang, W. Chu, H. Zhang, R. Zou and D. Xia, *Adv. Mater.*, 2018, **30**, 1707255.
53 K. Ku, J. Hong, H. Kim, H. Park, W. M. Seong, S.-K. Jung, G. Yoon, K.-Y. Park, H. Kim and K. Kang, *Adv. Energy Mater.*, 2018, **8**, 1800606.
54 J. L. Shi, D. D. Xiao, M. Ge, X. Yu, Y. Chu, X. Huang, X. D. Zhang, Y. X. Yin, X. Q. Yang, Y. G. Guo, L. Gu and L. J. Wan, *Adv. Mater.*, 2018, **30**, 1705575.
55 Y. You, H. Celio, J. Li, A. Dolocan and A. Manthiram, *Angew. Chem., Int. Ed.*, 2018, **57**, 6480–6485.
56 M. Chen, Z. Pan, X. Jin, Z. Chen, Y. Zhong, X. Wang, Y. Qiu, M. Xu, W. Li and Y. Zhang, *J. Mater. Chem. A*, 2019, **7**, 4494–4504.
57 Y. Zheng, L. Chen, Y. Su, J. Tan, L. Bao, Y. Lu, J. Wang, R. Chen, S. Chen and F. Wu, *J. Mater. Chem. A*, 2017, **5**, 24292–24298.
58 E. M. Erickson, H. Sclar, F. Schipper, J. Liu, R. Tian, C. Ghanty, L. Burstein, N. Leifer, J. Grinblat, M. Talianker, J.-Y. Shin, J. K. Lampert, B. Markovsky, A. I. Frenkel and D. Aurbach, *Adv. Energy Mater.*, 2017, **7**, 1700708.
59 P. Kumar Nayak, J. Grinblat, E. Levi, T. R. Penki, M. Levi, Y.-K. Sun, B. Markovsky and D. Aurbach, *ACS Appl. Mater. Interfaces*, 2016, **9**, 4309–4319.
60 T. R. Penki, P. K. Nayak, E. Levi, J. Grinblat, Y. Elias, S. Luski, B. Markovsky and D. Aurbach, *ChemElectroChem*, 2018, **5**, 1137–1146.
61 M. Zanella, G. Bertoni, I. R. Franchini, R. Brescia, D. Baranov and L. Manna, *Chem. Commun.*, 2011, **47**, 203–205.
62 A. K. Ganguli, A. Ganguly and S. Vaidya, *Chem. Soc. Rev.*, 2010, **39**, 474–485.
63 S. Sharma, N. Pal, P. K. Chowdhury, S. Sen and A. K. Ganguli, *J. Am. Chem. Soc.*, 2012, **134**, 19677–19684.
64 H. B. Lin, Y. M. Zhang, H. B. Rong, S. W. Mai, J. N. Hu, Y. H. Liao, L. D. Xing, M. Q. Xu, X. P. Li and W. S. Li, *J. Mater. Chem. A*, 2014, **2**, 11987.
65 M. C. Gregorio, P. Ranjan, L. Houben, L. J. W. Shimon, K. Rechav, M. Lahav and M. E. van der Boom, *J. Am. Chem. Soc.*, 2018, **140**, 9132–9139.
66 K. Luo, M. R. Roberts, R. Hao, N. Guerrini, D. M. Pickup, Y. S. Liu, K. Edstrom, J. Guo, A. V. Chadwick, L. C. Duda and P. G. Bruce, *Nat. Chem.*, 2016, **8**, 684–691.
67 P. E. Pearce, A. J. Perez, G. Rousse, M. Saubanère, D. Batuk, D. Foix, E. McCalla, A. M. Abakumov, G. Van Tendeloo, M.-L. Doublet and J.-M. Tarascon, *Nat. Mater.*, 2017, **16**, 580–586.
68 H. Yu, Y. G. So, Y. Ren, T. Wu, G. Guo, R. Xiao, J. Lu, H. Li, Y. Yang, H. Zhou, R. Wang, K. Amine and Y. Ikuhara, *J. Am. Chem. Soc.*, 2018, **140**, 15279–15289.
69 S. Zhang, J. Chen, T. Tang, Y. Jiang, G. Chen, Q. Shao, C. Yan, T. Zhu, M. Gao, Y. Liu and H. Pan, *J. Mater. Chem. A*, 2018, **6**, 3610–3624.
70 J. Zheng, M. Gu, A. Genc, J. Xiao, P. Xu, X. Chen, Z. Zhu, W. Zhao, L. Pullan, C. Wang and J. G. Zhang, *Nano Lett.*, 2014, **14**, 2628–2635.
71 G. Assat, D. Foix, C. Delacourt, A. Iadecola, R. Dedryvère and J.-M. Tarascon, *Nat. Commun.*, 2017, **8**, 2219.
72 P. K. Nayak, T. R. Penki, B. Markovsky and D. Aurbach, *ACS Energy Lett.*, 2017, **2**, 544–548.
73 B. Qiu, M. Zhang, Y. Xia, Z. Liu and Y. S. Meng, *Chem. Mater.*, 2017, **29**, 908–915.
74 S. Hy, F. Felix, J. Rick, W. N. Su and B. J. Hwang, *J. Am. Chem. Soc.*, 2014, **136**, 999–1007.